

Article

# Macroporous Activated Carbon Derived from Rapeseed Shell for Lithium–Sulfur Batteries

**Mingbo Zheng \*, Qin Hu, Songtao Zhang, Hao Tang, Lulu Li and Huan Pang \***

School of Chemistry and Chemical Engineering, Institute for Innovative Materials and Energy, Yangzhou University, Yangzhou 225009, Jiangsu, China; huqinchemistry@foxmail.com (Q.H.); teeth.h@163.com (S.Z.); 18361310292@163.com (H.T.); lilulu10000@163.com (L.L.)

\* Correspondence: mbzheng@yzu.edu.cn (M.Z.); panghuan@yzu.edu.cn (H.P.);  
Tel.: +86-514-8797-5230 (M.Z. & H.P.)

Received: 12 September 2017; Accepted: 28 September 2017; Published: 10 October 2017

**Abstract:** Lithium–sulfur batteries have drawn considerable attention because of their extremely high energy density. Activated carbon (AC) is an ideal matrix for sulfur because of its high specific surface area, large pore volume, small-size nanopores, and simple preparation. In this work, through KOH activation, AC materials with different porous structure parameters were prepared using waste rapeseed shells as precursors. Effects of KOH amount, activated temperature, and activated time on pore structure parameters of ACs were studied. AC sample with optimal pore structure parameters was investigated as sulfur host materials. Applied in lithium–sulfur batteries, the AC/S composite (60 wt % sulfur) exhibited a high specific capacity of  $1065 \text{ mAh g}^{-1}$  at  $200 \text{ mA g}^{-1}$  and a good capacity retention of 49% after 1000 cycles at  $1600 \text{ mA g}^{-1}$ . The key factor for good cycling stability involves the restraining effect of small-sized nanopores of the AC framework on the diffusion of polysulfides to bulk electrolyte and the loss of the active material sulfur. Results demonstrated that AC materials derived from rapeseed shells are promising materials for sulfur loading.

**Keywords:** biomass; activated carbon; sulfur hosts; lithium–sulfur battery

## 1. Introduction

Given the rapid development of portable electronics, electric vehicles, and smart grids, advanced electrochemical energy storage systems have been investigated extensively [1–11]. Lithium–sulfur (Li–S) batteries are expected to perform a significant role in the field of energy storage owing to its ultrahigh theoretical energy density of  $2500 \text{ Wh kg}^{-1}$ , environmental friendliness, and low cost [12–19]. However, in practical applications, Li–S batteries are usually hindered by problems originating from the sulfur cathode, metallic lithium anode, and electrolyte [20–23]. For the sulfur cathode, key problems mainly comprise three aspects: the low conductivity of sulfur and its discharge products, the diffusion of polysulfide ions, and the expansion of active material during electrochemical reaction [12–23]. To solve the abovementioned problems, one of the most effective methods is loading sulfur into electronically conductive frameworks with good structural stability [24–32]. Various nanoporous carbon materials, such as mesoporous carbon [33], porous graphene [34,35], porous carbon nanofibers [36,37], hollow carbon spheres [38], and activated carbon (AC) [39], have been widely studied as loading frameworks for sulfur. During electrochemical reaction, the carbon framework can not only provide a stable and conductive network for both sulfur and discharge products, but can also efficiently restrain the diffusion of polysulfides. Among porous carbon materials, AC, which features a large specific surface area, high pore volume, and small-size nanopores, is a highly promising framework for sulfur [39]. The large specific surface area and high pore volume can yield high mass loading and enhance the utilization of sulfur in electrochemical reactions, and nanopore structures with a small pore size can suppress the diffusion of polysulfide more efficiently [39].

The utilization and development of biomass resources are some of the most important research topics at present [40,41]. Biomass materials are rich in resources, widely available, renewable, and environmentally friendly. In recent years, considerable attention has been focused on AC prepared from biomass materials as a loading support for sulfur applied to the cathode of Li–S batteries [40–42]. Zhao et al. reported an AC material made from fish scale for sulfur loading [43]. The resulting nanocomposite cathode showed a discharge capacity of  $1039 \text{ mA h g}^{-1}$  at the first cycle and a reversible discharge capacity of  $1023 \text{ mA h g}^{-1}$  over 70 cycles at 1 C. Yin et al. reported an AC material by the utilization of coconut shell as a raw material [44]. The obtained AC/sulfur composite material possessed an initial capacity of  $878 \text{ mAh g}^{-1}$  and a reversible capacity of  $774 \text{ mAh g}^{-1}$  over 50 cycles at 0.1 C. In our previous works, AC materials were prepared from waste litchi shells and mango stones [45,46]. As-prepared AC/sulfur composite cathodes exhibited good electrochemical performance.

In this work, a series of AC materials was prepared using waste rapeseed shells as raw materials. Influences of KOH amount, activated temperature, and activated time on pore structure parameters of AC materials were studied. The AC sample with the maximum specific surface area ( $2090 \text{ m}^2 \text{ g}^{-1}$ ) and pore volume ( $1.28 \text{ cm}^3 \text{ g}^{-1}$ ) was applied as a loading framework for sulfur. When used as a cathode of a Li–S battery, the AC/sulfur composite exhibited high specific capacity and good capacity retention.

## 2. Materials and Methods

### 2.1. Preparation of Rapeseed Shell-Derived AC

Waste rapeseed shells were collected, cleaned, and dried. Two grams of dried rapeseed shell was impregnated in 5 wt % KOH solution for 12 h. After filtration, the obtained sample was dried at  $90^\circ\text{C}$ . Then, the rapeseed shell adsorbed with KOH was activated at  $800^\circ\text{C}$  of 1 h in Ar. After activation, the obtained sample was treated with 1 M HCl aqueous solution until pH reached 7 and was cleaned with deionized water. The last product was obtained after drying at  $80^\circ\text{C}$ . Concentration of KOH solution (2.5, 5, and 10 wt %), activation temperature ( $700^\circ\text{C}$ ;  $800^\circ\text{C}$ ), and activation time (1 and 3 h) were adjusted. Samples were named as AC-a-b-c, where “a” represents the concentration of KOH solution, “b” represents the activation temperature, and “c” represents the activation time.

### 2.2. Preparation of AC/S Composite

For the preparation of AC/S composite, sublimed sulfur (Aladdin, with a purity of >99.95%) and AC powders with a weight ratio of 60:40 were fully mixed and ground in a mortar. Then, the obtained mixture was sealed in an autoclave with a Teflon vessel. After 12 h of heat treatment at  $155^\circ\text{C}$ , the AC/S composite was obtained.

### 2.3. Material Characterization

Scanning electron microscopy (SEM) was performed on a JEOL JSM-6701F instrument. Transmission electron microscopy (TEM) was performed on a JEOL JEM-2100 instrument. Micromeritics ASAP 2020 instrument was utilized to conduct nitrogen adsorption–desorption analysis. Bruker D8 powder X-ray diffractometer was utilized to collect X-ray diffraction (XRD) data. Thermogravimetric analysis (TGA) was performed with a PerkinElmer Pyris 1 thermal analysis instrument under  $\text{N}_2$  flow.

### 2.4. Electrochemical Characterization

To form the slurry, 80 wt % AC/S composite, 10 wt % Super P, and 10 wt % polyvinylidene difluoride were mixed in N-methylpyrrolidone solvent. For the working electrode, the slurry was coated on Al foil and dried at  $50^\circ\text{C}$  for 2 h. The loading mass of composite materials for each electrode was between  $1.0 \text{ mg cm}^{-2}$  to  $1.2 \text{ mg cm}^{-2}$ . Coin cells (CR2032) were assembled in an Ar-filled glove box with lithium as the counter electrode and Celgard 2250 film as the separator. The electrolyte

comprised 1 M *bis*(trifluoromethane)sulfonimide lithium in dimethoxyethane and dioxolane (volume ratio 1:1). A charge/discharge test was performed on a LAND CT-2001A apparatus. The specific capacity was calculated based on sulfur mass. Cyclic voltammetry (CV) measurements were performed on a Chenhua CHI 760D electrochemical workstation.

### 3. Results and Discussion

SEM characterization was used to investigate sample morphology. During the comparison of four samples, macropores could not be observed in AC-0-800-1 (Figure 1a). However, three-dimensional interconnecting macropores were observed in AC-2.5-800-1, AC-5-800-1, and AC-10-800-1 samples (Figure 1b–d). Thus, macropores were formed from activation reaction of KOH. As the concentration of KOH increased, the macropore walls of AC became thinner until they collapsed. The macroporous structure of AC is conducive to the infiltration of sulfur into nanopores of AC during the preparation of sulfur/AC composite. TEM image of AC-5-800-1 also proved the macroporous structure of AC (Figure 1e). Furthermore, high-magnification TEM image exhibited that the macropore wall contained significant amounts of small-sized nanopores (Figure 1f). Abundant nanopores are beneficial for a homogenous distribution of sulfur.

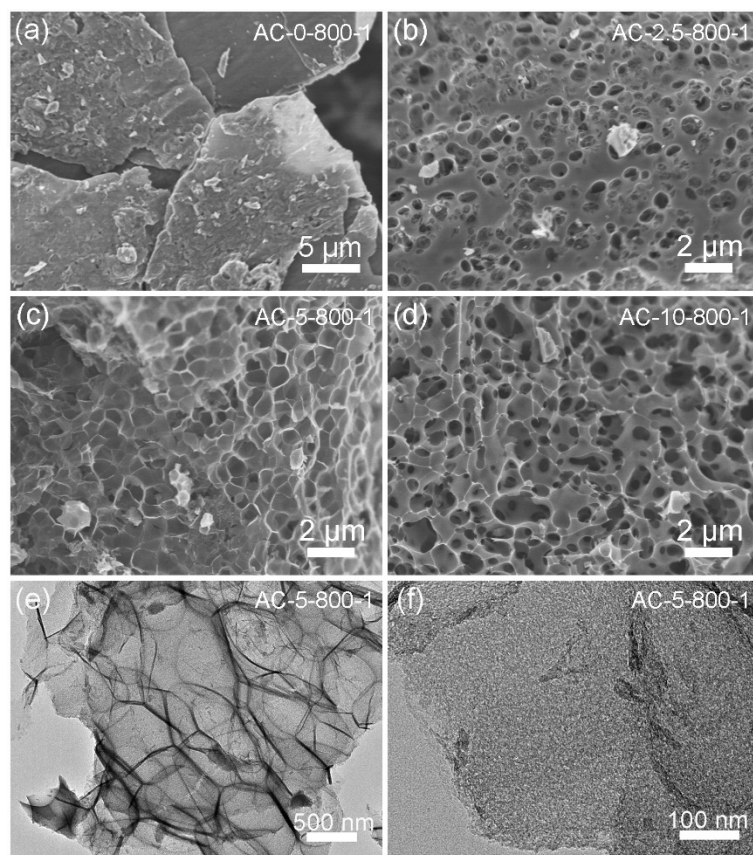


**Figure 1.** SEM images of (a) Activated carbon (AC)-0-800-1, (b) AC-2.5-800-1, (c) AC-5-800-1, (d) AC-10-800-1; (e,f) TEM images of AC-5-800-1.

The pore structure of the AC samples was analyzed by the N<sub>2</sub> isotherm adsorption–desorption method. As presented in Figure 2a,c, all samples showed combined isotherms between type I and type IV behavior. According to the classification of the International Union of Pure and Applied Chemistry, type I corresponds to adsorption on microporous solids, whereas type IV corresponds to adsorption on mesoporous solids, indicating the presence of both of micro- and mesoporous structures in the AC

samples. The high nitrogen uptake at low relative pressure of less than 0.1 in the adsorption branch of AC samples corresponded to a large amount of micropores. During this process, monolayer adsorption occurred, owing to the strong interaction between the nitrogen molecules and the pore wall. After the relative pressure reached 0.1, the adsorbing amount continually increased with increasing relative pressure, indicating the occurrence of multi-layer adsorption in mesopores. A slight hysteresis loop can be observed at relative pressures from 0.4 to 0.55 for AC-5-800-1, AC-10-800-1, and AC-5-800-3; such loop is commonly related to capillary condensation in mesopores. When the relative pressure approached 0.9, a further increase in volume was detected, indicating the existence of macropores in the samples. Figure 2b,d illustrate the pore size distribution curves based on the Barrett–Joyner–Halenda (BJH) equation. AC samples exhibited a pore distribution at about 2 nm, corresponding to high amounts of micropores and small mesopores. Table 1 summarizes the pore structure parameters of the AC samples. The Brunauer–Emmett–Teller (BET) specific surface area and pore volume of the samples depended mainly on the amount of KOH and the activated temperature. In all samples, AC-5-800-1 exhibited the largest BET surface area and the highest pore volume.

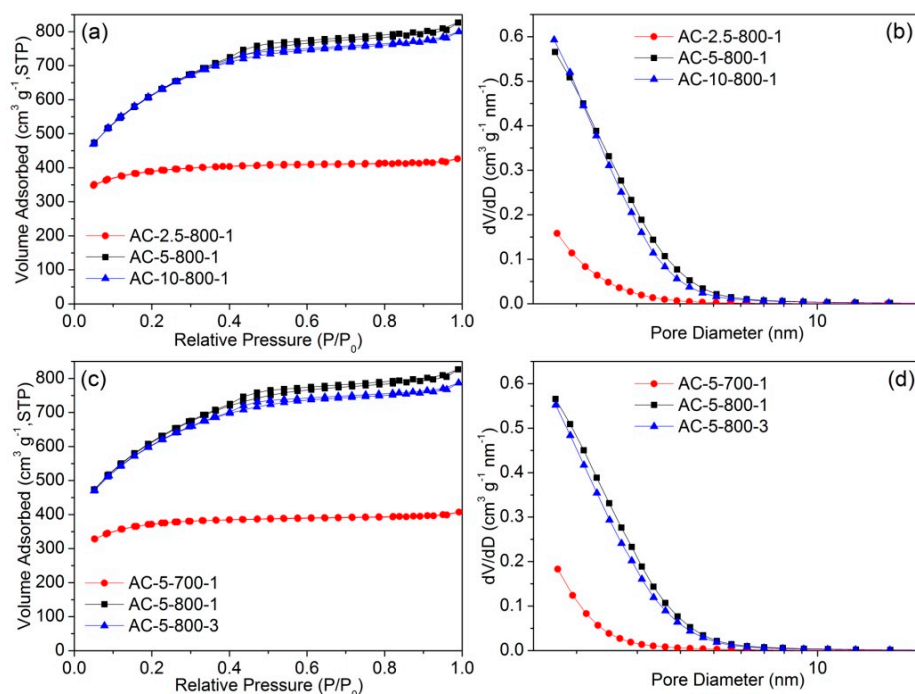


**Figure 2.** (a,c) N<sub>2</sub> adsorption–desorption isotherms of activated carbon (AC) samples; (b,d) Barrett–Joyner–Halenda (BJH) pore size distribution curves from adsorption branch of AC samples.

**Table 1.** Pore structure parameters of AC samples.

Samples	Brunauer–Emmett–Teller (BET) Surface Area (m <sup>2</sup> g <sup>-1</sup> )	Pore Volume (cm <sup>3</sup> g <sup>-1</sup> )	BJH Average Pore Size (nm)
AC-2.5-800-1	1211	0.66	2.8
AC-5-800-1	2090	1.28	2.7
AC-10-800-1	2082	1.24	2.6
AC-5-700-1	1157	0.63	2.7
AC-5-800-3	2035	1.22	2.7

AC-5-800-1 was further studied as a loading framework for sulfur due to its optimal pore structure parameters. For conciseness, AC-5-800-1 and the obtained sulfur/carbon composites are referred to as AC and AC/S composite in subsequent sections. Figure 3a presents the XRD patterns of pure

sulfur, AC, and AC/S composite. The AC sample showed a broad diffraction peak at approximately  $26^\circ$ , implying the amorphous character of AC. For the pure sulfur sample, sharp diffraction peaks indicated its crystal form. After impregnation into AC frameworks, sulfur-associated crystalline diffraction peaks were not observed in the AC/S sample. The results demonstrated that sulfur existed in an amorphous state inside the nanopores of AC. The sulfur content of the AC/S composite was analyzed by TGA measurements (Figure 3b). The weight of sublimed sulfur decreased sharply in the range of  $180\text{ }^\circ\text{C}$  to  $360\text{ }^\circ\text{C}$ . However, for AC/S composite, the loss of weight started at  $180\text{ }^\circ\text{C}$  and ended at  $390\text{ }^\circ\text{C}$ . Sulfur in the AC matrix was more thermally stable than that in the normal state, indicating the restraining effect of AC frameworks. TGA analysis indicated that the sulfur content in the composite closely approximated that of our design. AC/S composite was also characterized by  $\text{N}_2$  isotherm adsorption–desorption analysis. After the encapsulation of sulfur into AC nanopores, the nitrogen absorption volume decreased markedly (Figure 3c). For the BJH pore size distribution curve of AC/S composite, the main peak significantly decreased (Figure 3d), demonstrating that sulfur deeply impregnated the AC nanopores. The pore volume and BET surface area of AC/S composite measured  $0.03\text{ cm}^3\text{ g}^{-1}$  and  $10\text{ m}^2\text{ g}^{-1}$ , respectively. Notable diminution of these two parameters also suggests that sulfur was infused into the nanopores of the AC hosts.

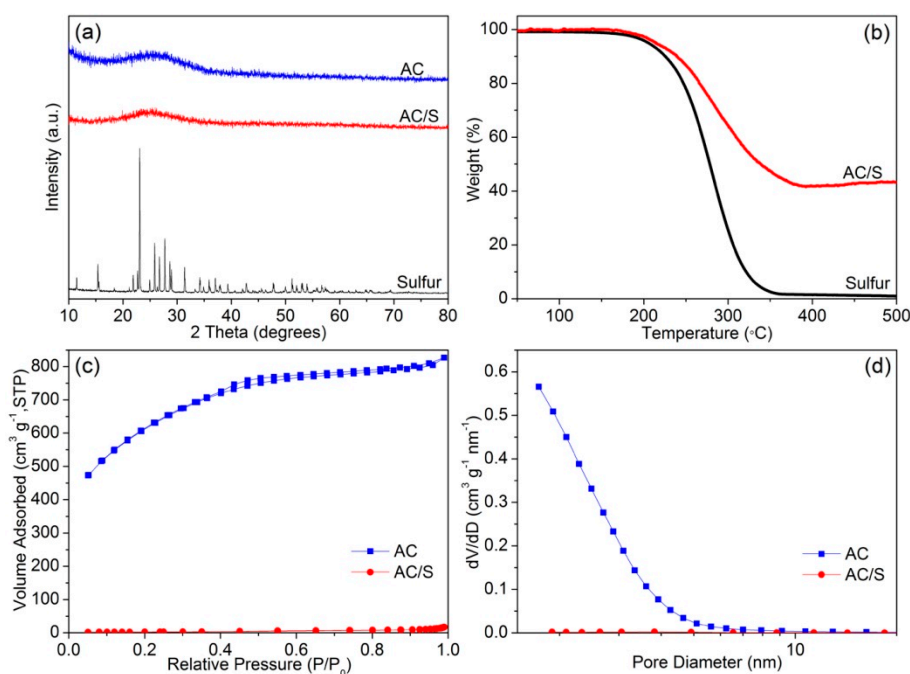


**Figure 3.** (a) XRD patterns of elemental sulfur, AC, and activated carbon/S (AC/S) composite; (b) Thermogravimetric analysis (TGA) profiles of elemental sulfur and AC/S composite; (c)  $\text{N}_2$  adsorption–desorption isotherms and (d) BJH pore size distribution curves from the adsorption branch of AC and AC/S composite.

Figure 4a,b exhibit SEM images of AC/S composite at various magnifications. The macroporous structure of AC was partially destroyed due to the grinding treatment during the preparation of AC/S composite. Bulky sulfur was not observed on the surface of AC/S particles. Figure 4c–e present SEM images of the composite and corresponding energy dispersive spectroscopy (EDS) mapping for elemental carbon and sulfur. Sulfur was evenly dispersed in the AC/S composite.

To evaluate the electrochemical performance of AC/S composite, coin cells were assembled with AC/S composite as the cathode. Figure 5a shows CV curves of AC/S during the initial two cycles at  $0.05\text{ mV s}^{-1}$  from  $1.7\text{ V}$  to  $2.7\text{ V}$ . During the discharge process, two peaks at potentials of  $2.29$  and  $2.03\text{ V}$  corresponded to reductions of sulfur to soluble lithium polysulfides ( $\text{Li}_2\text{S}_n$ ,  $4 \leq n \leq 8$ ) and low-order

polysulfides to solid-state  $\text{Li}_2\text{S}_2/\text{Li}_2\text{S}$ . During the subsequent charge process, the sample showed two peaks at potentials of 2.33 and 2.36 V, corresponding to oxidations of  $\text{Li}_2\text{S}_2/\text{Li}_2\text{S}$  to  $\text{Li}_2\text{S}_n$  ( $4 \leq n \leq 8$ ) and  $\text{Li}_2\text{S}_n$  ( $4 \leq n \leq 8$ ) to sulfur, respectively [39]. Figure 5b shows typical voltage versus capacity curves at  $200 \text{ mA g}^{-1}$  for the first and second cycles. The discharge curves exhibit two plateaus, which can be ascribed to the multistep reduction of sulfur to lithium sulfides. The two plateaus coincide with the two peaks in CV curves obtained during the discharge process. The composite electrode delivered an initial discharge capacity of  $1065 \text{ mAh g}^{-1}$ . The cell was further tested at various charge/discharge current densities. With increasing current densities, voltage versus capacity curves for AC/S composite maintained the typical two-plateau characteristic (Figure 5c). Figure 5d shows that AC/S composite delivered specific discharge capacities of 980, 840, 750, 680, and  $590 \text{ mA h g}^{-1}$  at  $200, 400, 800, 1600$  and  $3200 \text{ mA g}^{-1}$ , respectively. Therefore, the AC/S composite exhibited good rate performance.

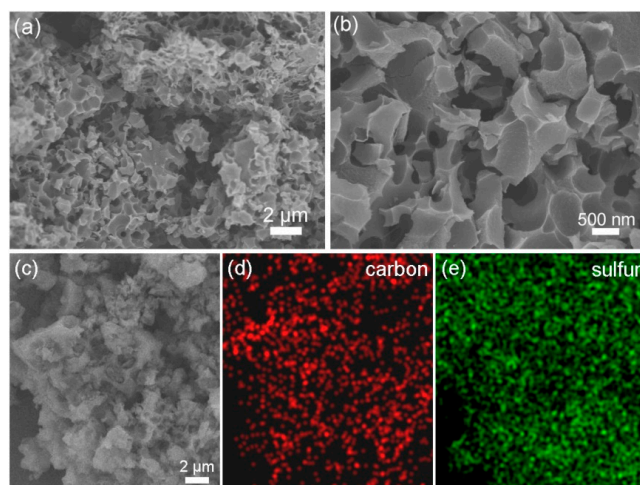


**Figure 4.** (a,b) SEM images of AC/S composite at various magnifications; (c) SEM image of AC/S composite and corresponding energy dispersive spectroscopy (EDS) mapping of elemental (d) carbon and (e) sulfur.

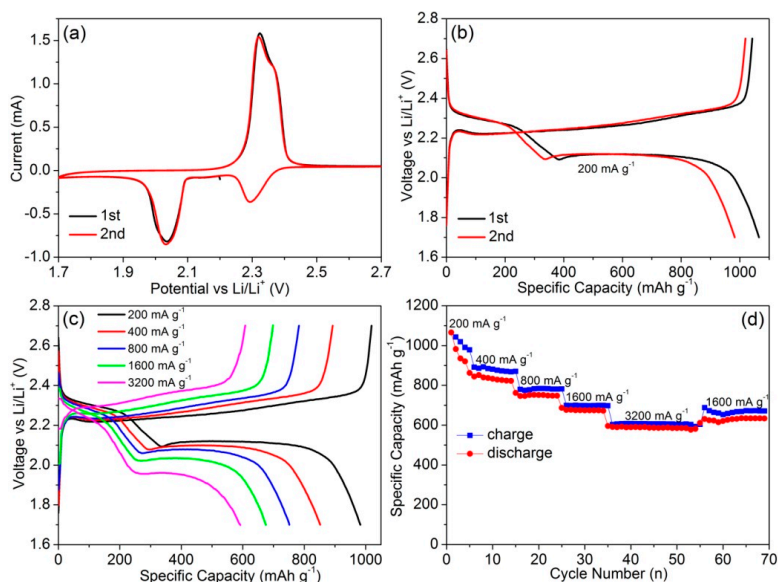


**Figure 5.** (a) Cyclic voltammetry (CV) curves of the AC/S composite cathode in the initial two cycles at  $0.05 \text{ mV s}^{-1}$ ; (b) galvanostatic charge/discharge curves of AC/S composite cathode at  $200 \text{ mA g}^{-1}$ ; (c) galvanostatic charge/discharge curves of the AC/S composite cathode at various current densities; (d) rate performance of AC/S composite.

To demonstrate long cycle performance, the cell was tested at  $800 \text{ mA g}^{-1}$  for 500 cycles under the galvanostatic mode (Figure 6a). The initial specific discharge capacity reached  $942 \text{ mA h g}^{-1}$ , and the maximum reversible discharge capacity of  $819 \text{ mAh g}^{-1}$  was obtained in the second cycle. The cells still possessed a reversible discharge capacity of  $486 \text{ mAh g}^{-1}$  after 500 cycles, representing a high capacity retention of 59%. To further suppress the polysulfide shuttle, 1 wt % LiNO<sub>3</sub> was added to the electrolyte (Figure 6b). After 500 cycles, the average Coulombic efficiency of the sample reached 97%, with LiNO<sub>3</sub> as an electrolyte additive. At  $1600 \text{ mA g}^{-1}$ , an initial discharge capacity of  $906 \text{ mAh g}^{-1}$  can be obtained. A maximum reversible discharge capacity of  $792 \text{ mAh g}^{-1}$  was achieved in the second cycle (Figure 6c). The specific capacity remained at  $385 \text{ mA h g}^{-1}$  after 1000 cycles (49% capacity retention). The composite cathode delivered an extremely low decay rate of 0.051% per cycle, indicating notable long-term cycle performance. This superior cycle stability was ascribed to the restraining effect for the diffusion of polysulfides to bulk electrolyte and the loss of active material sulfur by the AC matrix with a small-size nanopore structure. During the 1000 cycles, charge/discharge curves maintained the two-plateau characteristic of Li–S batteries (Figures S1–S3). In addition, the AC/S composite displayed good cycling performance in comparison with other porous carbon/sulfur composite cathodes (Table 2).

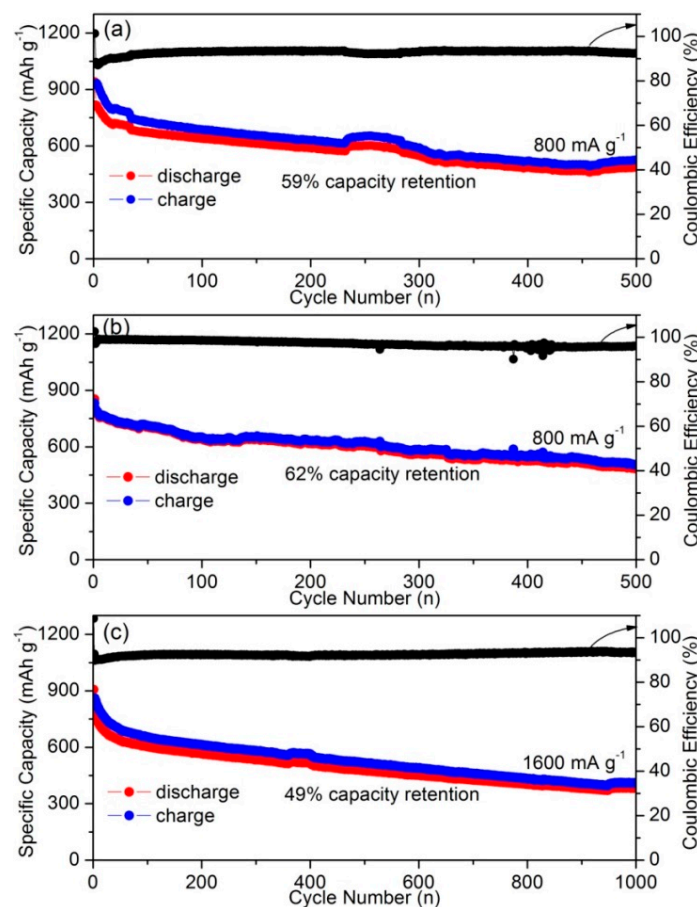


**Figure 6.** Long-term cycle performance and coulombic efficiencies of AC/S composite. (a) After 500 cycles under  $800 \text{ mA g}^{-1}$ ; (b) after 500 cycles under  $800 \text{ mA g}^{-1}$  with the addition of 1 wt % LiNO<sub>3</sub> in electrolyte; (c) after 1000 cycles under  $1600 \text{ mA g}^{-1}$  (the sudden increase of capacity during cycling is due to the increase in room temperature).

**Table 2.** Comparison of porous structure parameters and discharge capacities of porous carbon materials for Li–S batteries.

Carbon Host Materials	Surface Area ( $\text{m}^2 \text{ g}^{-1}$ )	Pore Volume ( $\text{cm}^3 \text{ g}^{-1}$ )	S (wt %)	Initial Capacity ( $\text{mA h g}^{-1}$ )	Capacity Retention ( $\text{mA h g}^{-1}$ )	Cycle Number	Current Density ( $\text{mA g}^{-1}$ )	Refs.
AC from coconut shell	677	0.29	60	878	774	50	167.5	[44]
Microporous carbon from coconut shell	1600	0.66	45.8	1458	411	400	335	[47]
Meso/micro/macroporous carbon	2157	2.26	63	1265	643	50	400	[48]
Mesoporous carbon sphere	1270	4.1	60	1388	857	100	335	[49]
Micro/mesoporous activated graphene	2995	2.14	75	620	471	200	1675	[50]
Graphene-based layered porous carbon	2500	1.94	68	886	620	100	837.5	[51]
Honeycomb carbon	614	1.34	66	923	564	100	3350	[52]
AC from rapeseed shell	2090	1.28	60	942	486	500	800	This work

#### 4. Conclusions

Through the KOH activation method, AC materials with various pore structure parameters were fabricated using waste rapeseed shells as precursors. Influences of the amount of KOH, activated temperature, and activated time on the pore structure parameters of ACs were studied. The as-prepared AC-800-5-1 sample exhibited the highest specific surface area of  $2092 \text{ m}^2 \text{ g}^{-1}$  and the largest pore volume of  $1.28 \text{ cm}^3 \text{ g}^{-1}$  among all of the samples. After the infusion of sulfur into nanopores of AC-800-5-1, the obtained AC/sulfur composite exhibited high specific capacity, good rate performance, and long cycle performance as a cathode of Li–S batteries. Our results indicate that AC materials derived from rapeseed shell provide a promising, conductive framework for sulfur cathodes. Furthermore, the material offers potential applications in the fields of adsorption and catalyst supports.

**Supplementary Materials:** The following are available online at <http://www.mdpi.com/2076-3417/7/10/1036/s1>, Figure S1: Galvanostatic charge/discharge profiles of AC/S composite over 500 cycles at  $800 \text{ mA g}^{-1}$ , Figure S2: Galvanostatic charge/discharge profiles of AC/S composite over 500 cycles at  $800 \text{ mA g}^{-1}$  with 1 wt %  $\text{LiNO}_3$  as electrolyte additive, Figure S3: Galvanostatic charge/discharge profiles of AC/S composite over 1000 cycles at  $1600 \text{ mA g}^{-1}$ .

**Acknowledgments:** This work was supported by the Program for the National Natural Science Foundation of China (NSFC-51202106, 21671170 and 21201010), Project for the Natural Science Research of the Institutions of Higher Learning in Jiangsu Province (17KJB150045), and New Century Excellent Talents of the University in China (grant no. NCET-13-0645), Innovation Scientists and Technicians Troop Construction Projects of Henan Province (164200510018), Plan for Scientific Innovation Talent of Henan Province, Program for Innovative Research Team (in Science and Technology) in University of Henan Province (14IRTSTHN004, 16IRTSTHN003), the Science & Technology Foundation of Henan Province (122102210253 and 13A150019), the Science & Technology Foundation of Jiangsu Province (BK20150438), the Six Talent Plan (2015-XCL-030), and the China Postdoctoral Science Foundation (2012M521115). We also acknowledge the Priority Academic Program Development of Jiangsu Higher Education Institutions and the technical support we received at the Testing Center of Yangzhou University.

**Author Contributions:** M.B.Z., Q.H. and H.P. conceived and designed the experiments; M.B.Z., Q.H. and S.T.Z. performed the experiments; M.B.Z., Q.H., S.T.Z., H.T., L.L.L. and H.P. analyzed the data; M.B.Z. wrote the paper.

**Conflicts of Interest:** The authors declare no conflict of interest.

#### References

1. Song, B.; Lai, M.O.; Liu, Z.; Liu, H.; Lu, L. Graphene-based surface modification on layered Li-rich cathode for high-performance Li-ion batteries. *J. Mater. Chem. A* **2013**, *1*, 9954–9965. [[CrossRef](#)]
2. Liu, S.; Feng, J.; Bian, X.; Liu, J.; Xu, H.; An, Y. A controlled red phosphorus@Ni–P core@shell nanostructure as an ultralong cycle-life and superior high-rate anode for sodium-ion batteries. *Energy Environ. Sci.* **2017**, *10*, 1222–1233. [[CrossRef](#)]
3. Demirocak, D.; Srinivasan, S.; Stefanakos, E. A review on nanocomposite materials for rechargeable Li-ion batteries. *Appl. Sci.* **2017**, *7*, 731. [[CrossRef](#)]
4. Lee, D.; Ahn, S. Investigation of laser cutting width of  $\text{LiCoO}_2$  coated aluminum for lithium-ion batteries. *Appl. Sci.* **2017**, *7*, 914. [[CrossRef](#)]

5. Yang, Q.; Lu, Z.; Li, T.; Sun, X.; Liu, J. Hierarchical construction of core-shell metal oxide nanoarrays with ultrahigh areal capacitance. *Nano Energy* **2014**, *7*, 170–178. [[CrossRef](#)]
6. Wu, X.; Lu, Z.; Zhu, W.; Yang, Q.; Zhang, G.; Liu, J.; Sun, X. High-performance aqueous battery with double hierarchical nanoarrays. *Nano Energy* **2014**, *10*, 229–234. [[CrossRef](#)]
7. Li, B.; Gu, P.; Feng, Y.; Zhang, G.; Huang, K.; Xue, H.; Pang, H. Ultrathin nickel-cobalt phosphate 2D nanosheets for electrochemical energy storage under aqueous/solid-state electrolyte. *Adv. Funct. Mater.* **2017**, *27*, 1605784. [[CrossRef](#)]
8. Zheng, S.; Li, X.; Yan, B.; Hu, Q.; Xu, Y.; Xiao, X.; Xue, H.; Pang, H. Transition-metal (Fe, Co, Ni) based metal-organic frameworks for electrochemical energy storage. *Adv. Energy Mater.* **2017**, *1602733*. [[CrossRef](#)]
9. Jiang, J.; He, P.; Tong, S.; Zheng, M.; Lin, Z.; Zhang, X.; Shi, Y.; Zhou, H. Ruthenium functionalized graphene aerogels with hierarchical and three-dimensional porosity as a free-standing cathode for rechargeable lithium-oxygen batteries. *NPG Asia Mater.* **2016**, *8*, e239. [[CrossRef](#)]
10. Chen, M.; Li, W.; Shen, X.; Diao, G. Fabrication of core-shell  $\alpha$ -Fe<sub>2</sub>O<sub>3</sub>@Li<sub>4</sub>Ti<sub>5</sub>O<sub>12</sub> composite and its application in the lithium-ion batteries. *ACS Appl. Mater. Interfaces* **2014**, *6*, 4514–4523. [[CrossRef](#)] [[PubMed](#)]
11. Zhou, M.; Lu, F.; Shen, X.; Xia, W.; He, H.; Zeng, X. One-pot construction of three dimensional CoMoO<sub>4</sub>/Co<sub>3</sub>O<sub>4</sub> hybrid nanostructures and their application in supercapacitors. *J. Mater. Chem. A* **2015**, *3*, 21201–21210. [[CrossRef](#)]
12. Hu, G.; Sun, Z.; Shi, C.; Fang, R.; Chen, J.; Hou, P.; Liu, C.; Cheng, H.-M.; Li, F. A sulfur-rich copolymer@CNT hybrid cathode with dual-confinement of polysulfides for high-performance lithium-sulfur batteries. *Adv. Mater.* **2017**, *29*, 1603835. [[CrossRef](#)] [[PubMed](#)]
13. Sun, Z.; Zhang, J.; Yin, L.; Hu, G.; Fang, R.; Cheng, H.-M.; Li, F. Conductive porous vanadium nitride/graphene composite as chemical anchor of polysulfides for lithium-sulfur batteries. *Nat. Commun.* **2017**, *8*, 14627. [[CrossRef](#)] [[PubMed](#)]
14. Bai, S.; Liu, X.; Zhu, K.; Wu, S.; Zhou, H. Metal-organic framework-based separator for lithium-sulfur batteries. *Nat. Energy* **2016**, *1*, 16094. [[CrossRef](#)]
15. Peng, H.-J.; Huang, J.-Q.; Liu, X.-Y.; Cheng, X.-B.; Xu, W.-T.; Zhao, C.-Z.; Wei, F.; Zhang, Q. Healing high-loading sulfur electrodes with unprecedented long cycling life: Spatial heterogeneity control. *J. Am. Chem. Soc.* **2017**, *139*, 8458–8466. [[CrossRef](#)] [[PubMed](#)]
16. Wang, T.; Kretschmer, K.; Choi, S.; Pang, H.; Xue, H.; Wang, G. Fabrication methods of porous carbon materials and separator membranes for lithium-sulfur batteries: Development and future perspectives. *Small Methods* **2017**, *1*, 1700089. [[CrossRef](#)]
17. Yin, Y.-X.; Xin, S.; Guo, Y.-G.; Wan, L.-J. Lithium-sulfur batteries: Electrochemistry, materials, and prospects. *Angew. Chem. Int. Ed.* **2013**, *52*, 13186–13200. [[CrossRef](#)] [[PubMed](#)]
18. Wang, H.; Zhou, T.; Li, D.; Gao, H.; Gao, G.; Du, A.; Liu, H.; Guo, Z. Ultrathin cobaltosic oxide nanosheets as an effective sulfur encapsulation matrix with strong affinity toward polysulfides. *ACS Appl. Mater. Interfaces* **2017**, *9*, 4320–4325. [[CrossRef](#)] [[PubMed](#)]
19. Wang, H.; Zhang, W.; Liu, H.; Guo, Z. A strategy for configuration of an integrated flexible sulfur cathode for high-performance lithium-sulfur batteries. *Angew. Chem. Int. Ed.* **2016**, *55*, 3992–3996. [[CrossRef](#)] [[PubMed](#)]
20. Ni, L.; Wu, Z.; Zhao, G.; Sun, C.; Zhou, C.; Gong, X.; Diao, G. Core-shell structure and interaction mechanism of  $\gamma$ -MnO<sub>2</sub> coated sulfur for improved lithium-sulfur batteries. *Small* **2017**, *13*, 1603466. [[CrossRef](#)] [[PubMed](#)]
21. Liu, W.; Jiang, J.; Yang, K.R.; Mi, Y.; Kumaravadivel, P.; Zhong, Y.; Fan, Q.; Weng, Z.; Wu, Z.; Cha, J.J.; et al. Ultrathin dendrimer-graphene oxide composite film for stable cycling lithium-sulfur batteries. *Proc. Natl. Acad. Sci. USA* **2017**, *114*, 3578–3583. [[CrossRef](#)] [[PubMed](#)]
22. Wang, L.; Liu, J.; Yuan, S.; Wang, Y.; Xia, Y. To mitigate self-discharge of lithium-sulfur batteries by optimizing ionic liquid electrolytes. *Energy Environ. Sci.* **2016**, *9*, 224–231. [[CrossRef](#)]
23. Ma, Z.; Huang, X.; Jiang, Q.; Huo, J.; Wang, S. Enhanced cycling stability of lithium-sulfur batteries by electrostatic-interaction. *Electrochim. Acta* **2015**, *182*, 884–890. [[CrossRef](#)]
24. Zhang, C.; Yang, Q.-H. Packing sulfur into carbon framework for high volumetric performance lithium-sulfur batteries. *Sci. China Mater.* **2015**, *58*, 349–354. [[CrossRef](#)]
25. Liu, M.; Yang, Z.; Sun, H.; Lai, C.; Zhao, X.; Peng, H.; Liu, T. A hybrid carbon aerogel with both aligned and interconnected pores as interlayer for high-performance lithium-sulfur batteries. *Nano Res.* **2016**, *9*, 3735–3746. [[CrossRef](#)]

26. Ding, Y.-L.; Kopold, P.; Hahn, K.; van Aken, P.A.; Maier, J.; Yu, Y. Facile solid-state growth of 3D well-interconnected nitrogen-rich carbon nanotube-graphene hybrid architectures for lithium-sulfur batteries. *Adv. Funct. Mater.* **2016**, *26*, 1112–1119. [[CrossRef](#)]
27. Zhang, J.; Yang, C.-P.; Yin, Y.-X.; Wan, L.-J.; Guo, Y.-G. Sulfur encapsulated in graphitic carbon nanocages for high-rate and long-cycle lithium-sulfur batteries. *Adv. Mater.* **2016**, *28*, 9539–9544. [[CrossRef](#)] [[PubMed](#)]
28. Tang, C.; Li, B.-Q.; Zhang, Q.; Zhu, L.; Wang, H.-F.; Shi, J.-L.; Wei, F. CaO-templated growth of hierarchical porous graphene for high-power lithium-sulfur battery applications. *Adv. Funct. Mater.* **2016**, *26*, 577–585. [[CrossRef](#)]
29. Ma, Z.; Tao, L.; Liu, D.; Li, Z.; Zhang, Y.; Liu, Z.; Liu, H.; Chen, R.; Huo, J.; Wang, S. Ultrafine nano-sulfur particles anchored on in situ exfoliated graphene for lithium-sulfur batteries. *J. Mater. Chem. A* **2017**, *5*, 9412–9417. [[CrossRef](#)]
30. Li, Z.; Huang, Y.; Yuan, L.; Hao, Z.; Huang, Y. Status and prospects in sulfur-carbon composites as cathode materials for rechargeable lithium-sulfur batteries. *Carbon* **2015**, *92*, 41–63. [[CrossRef](#)]
31. Yu, H.; Li, H.; Yuan, S.; Yang, Y.; Zheng, J.; Hu, J.; Yang, D.; Wang, Y.; Dong, A. Three-dimensionally ordered, ultrathin graphitic-carbon frameworks with cage-like mesoporosity for highly stable Li-S batteries. *Nano Res.* **2017**, *10*, 2495–2507. [[CrossRef](#)]
32. Chen, S.; Sun, B.; Xie, X.; Mondal, A.K.; Huang, X.; Wang, G. Multi-chambered micro/mesoporous carbon nanocubes as new polysulfides reservoirs for lithium-sulfur batteries with long cycle life. *Nano Energy* **2015**, *16*, 268–280. [[CrossRef](#)]
33. Li, X.; Cao, Y.; Qi, W.; Saraf, L.V.; Xiao, J.; Nie, Z.; Mietek, J.; Zhang, J.-G.; Schwenzer, B.; Liu, J. Optimization of mesoporous carbon structures for lithium-sulfur battery applications. *J. Mater. Chem.* **2011**, *21*, 16603–16610. [[CrossRef](#)]
34. Li, N.; Zheng, M.; Lu, H.; Hu, Z.; Shen, C.; Chang, X.; Ji, G.; Cao, J.; Shi, Y. High-rate lithium-sulfur batteries promoted by reduced graphene oxide coating. *Chem. Commun.* **2012**, *48*, 4106–4108. [[CrossRef](#)] [[PubMed](#)]
35. Yuan, S.; Guo, Z.; Wang, L.; Hu, S.; Wang, Y.; Xia, Y. Leaf-like graphene-oxide-wrapped sulfur for high-performance lithium-sulfur battery. *Adv. Sci.* **2015**, *2*, 1500071. [[CrossRef](#)] [[PubMed](#)]
36. Zeng, L.; Pan, F.; Li, W.; Jiang, Y.; Zhong, X.; Yu, Y. Free-standing porous carbon nanofibers-sulfur composite for flexible Li-S battery cathode. *Nanoscale* **2014**, *6*, 9579–9587. [[CrossRef](#)] [[PubMed](#)]
37. Chen, S.; Huang, X.; Liu, H.; Sun, B.; Yeoh, W.; Li, K.; Zhang, J.; Wang, G. 3D hyperbranched hollow carbon nanorod architectures for high-performance lithium-sulfur batteries. *Adv. Energy Mater.* **2014**, *4*, 1301761. [[CrossRef](#)]
38. Chen, S.; Huang, X.; Sun, B.; Zhang, J.; Liu, H.; Wang, G. Multi-shelled hollow carbon nanospheres for lithium-sulfur batteries with superior performances. *J. Mater. Chem. A* **2014**, *2*, 16199–16207. [[CrossRef](#)]
39. Zheng, M.; Zhang, S.; Chen, S.; Lin, Z.; Pang, H.; Yu, Y. Activated Graphene with Tailored Pore Structure Parameters for Long Cycle-Life Lithium-Sulfur Batteries. Available online: <https://link.springer.com/article/10.1007%2Fs12274-017-1659-3> (accessed on 7 June 2017).
40. Yao, Y.; Wu, F. Naturally derived nanostructured materials from biomass for rechargeable lithium/sodium batteries. *Nano Energy* **2015**, *17*, 91–103. [[CrossRef](#)]
41. Imtiaz, S.; Zhang, J.; Zafar, Z.A.; Ji, S.; Huang, T.; Anderson, J.A.; Zhang, Z.; Huang, Y. Biomass-derived nanostructured porous carbons for lithium-sulfur batteries. *Sci. China Mater.* **2016**, *59*, 389–407. [[CrossRef](#)]
42. Huang, Y.; Zheng, M.; Lin, Z.; Zhao, B.; Zhang, S.; Yang, J.; Zhu, C.; Zhang, H.; Sun, D.; Shi, Y. Flexible cathodes and multifunctional interlayers based on carbonized bacterial cellulose for high-performance lithium-sulfur batteries. *J. Mater. Chem. A* **2015**, *3*, 10910–10918. [[CrossRef](#)]
43. Zhao, S.; Li, C.; Wang, W.; Zhang, H.; Gao, M.; Xiong, X.; Wang, A.; Yuan, K.; Huang, Y.; Wang, F. A novel porous nanocomposite of sulfur/carbon obtained from fish scales for lithium-sulfur batteries. *J. Mater. Chem. A* **2013**, *1*, 3334–3339. [[CrossRef](#)]
44. Yin, Y.; Ma, C.; Cao, Z.; Sun, Z.; Jia, Y.; Yang, S. A novel sulfur/carbon composite for low cost lithium-sulfur batteries with high cycling stability. *RSC Adv.* **2014**, *4*, 28871–28874. [[CrossRef](#)]
45. Zhang, S.; Zheng, M.; Lin, Z.; Li, N.; Liu, Y.; Zhao, B.; Pang, H.; Cao, J.; He, P.; Shi, Y. Activated carbon with ultrahigh specific surface area synthesized from natural plant material for lithium-sulfur batteries. *J. Mater. Chem. A* **2014**, *2*, 15889–15896. [[CrossRef](#)]

46. Zhang, S.; Zheng, M.; Lin, Z.; Zang, R.; Huang, Q.; Xue, H.; Cao, J.; Pang, H. Mango stone-derived activated carbon with high sulfur loading as a cathode material for lithium-sulfur batteries. *RSC Adv.* **2016**, *6*, 39918–39925. [[CrossRef](#)]
47. Helen, M.; Reddy, M.A.; Diemant, T.; Golla-Schindler, U.; Behm, R.J.; Kaiser, U.; Fichtner, M. Single step transformation of sulphur to  $\text{Li}_2\text{S}_2/\text{Li}_2\text{S}$  in Li-S batteries. *Sci. Rep.* **2015**, *5*, 12146. [[CrossRef](#)] [[PubMed](#)]
48. Wei, S.; Zhang, H.; Huang, Y.; Wang, W.; Xia, Y.; Yu, Z. Pig bone derived hierarchical porous carbon and its enhanced cycling performance of lithium-sulfur batteries. *Energy Environ. Sci.* **2011**, *4*, 736–740. [[CrossRef](#)]
49. Wang, D.; Fu, A.; Li, H.; Wang, Y.; Guo, P.; Liu, J.; Zhao, X.S. Mesoporous carbon spheres with controlled porosity for high-performance lithium-sulfur batteries. *J. Power Sources* **2015**, *285*, 469–477. [[CrossRef](#)]
50. You, Y.; Zeng, W.; Yin, Y.-X.; Zhang, J.; Yang, C.-P.; Zhu, Y.; Guo, Y.-G. Hierarchically micro/mesoporous activated graphene with a large surface area for high sulfur loading in Li-S batteries. *J. Mater. Chem. A* **2015**, *3*, 4799–4802. [[CrossRef](#)]
51. Yang, X.; Zhang, L.; Zhang, F.; Huang, Y.; Chen, Y. Sulfur-infiltrated graphene-based layered porous carbon cathodes for high-performance lithium-sulfur batteries. *ACS Nano* **2014**, *8*, 5208–5215. [[CrossRef](#)] [[PubMed](#)]
52. Qu, Y.; Zhang, Z.; Zhang, X.; Ren, G.; Wang, X.; Lai, Y.; Liu, Y.; Li, J. Synthesis of hierarchical porous honeycomb carbon for lithium-sulfur battery cathode with high rate capability and long cycling stability. *Electrochim. Acta* **2014**, *137*, 439–446. [[CrossRef](#)]



© 2017 by the authors. Licensee MDPI, Basel, Switzerland. This article is an open access article distributed under the terms and conditions of the Creative Commons Attribution (CC BY) license (<http://creativecommons.org/licenses/by/4.0/>).